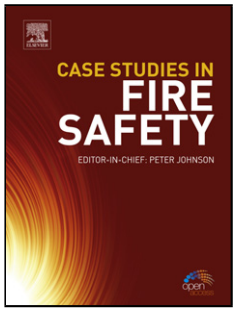

Title: Anodising and Corrosion resistance of AA 7050 Friction Stir Welds

Author: Pedro Atz Dick Gerhard H. Knörnschild Luís F.P. Dick

PII: S0010-938X(16)30995-7
DOI: http://dx.doi.org/doi:10.1016/j.corsci.2016.10.015
Reference: CS 6913

To appear in:

Received date: 20-7-2016
Revised date: 18-10-2016
Accepted date: 20-10-2016

Please cite this article as: Pedro Atz Dick, Gerhard H.Knörnschild, Luís F.P.Dick, Anodising and Corrosion resistance of AA 7050 Friction Stir Welds, Corrosion Science http://dx.doi.org/10.1016/j.corsci.2016.10.015

Anodising and Corrosion resistance of AA 7050 Friction Stir Welds

Pedro Atz Dick[a], Gerhard H. Knörnschild[a], Luís F. P. Dick [a,]*.

[a] Laboratório de Processos Eletroquímicos e Corrosão, Universidade Federal do Rio Grande do Sul, Av. Bento Gonçalves 9500, Prédio 75, CEP: 91501.970, Porto Alegre, Brazil

* Corresponding author: Tel: +55 5133087537

E-mail addresses: *pedro.dick@gmail.com* (P.A.D), *gerhard.hans@ufrgs.br* (G.H.K), *lfdick@ufrgs.br* (L.F.P.D).

Highlights

• Sulphuric Anodizing films of AA7050 friction stir welds are 25% thinner on the nugget zone.

• Semicoherent $MgZn_2$ precipitates locally pin the formation of anodic oxide film.

• Coarse Al_7Cu_2Fe precipitates anodize irregularly and produce locally thicker films.

• Localized corrosion occurs preferentially on the nugget zone and is related to the thinner oxide film and irregular anodizing on stirring voids.

Abstract

The influence of friction stir welding on the sulphuric anodising and corrosion of AA7050 was studied in 0.1M NaCl by the scanning vibrating electrode technique under simultaneous polarization. The oxide films obtained were characterized by scanning electron microscopy. The porous oxide films are up to 25% thicker on the thermomechanically and heat affected zones and 25% thinner on the nugget. This thinner defective oxide film explains the lower pitting resistance of the nugget zone. Individual pit current transients were indirectly determined from current maps. However, the calculated values are lower than expected, due to underestimation of electrolyte conductivity near pits.

Keywords: A. AA7050-T76511; B. Scanning Vibrating Electrode Technique; B. SVET under simultaneous polarization; C. Friction stir welding; C. Anodising; C. Pitting.

1. Introduction

Friction Stir Welding (FSW) is a solid-state joining technique with various advantages when compared to other welding methods, being therefore a very important and promising process for the aerospace industry. This technique is particularly well suited for high-strength aluminium alloys, such as the highly alloyed 2XXX and 7XXX series, which undergo well defined precipitation hardening heat treatments, and which suffer significant loss of mechanical properties and occurrence of defects if welded by methods that involve fusion [1]. In FSW, a high quality, almost defect-free joint is created by the friction between a non-consumable rotating tool and the plates to be joined. The heat resultant from friction and intense plastic deformation softens the metal and the stirring of material produces the joint, without reaching the melting temperature of the base material (BM) [2].

The final microstructure obtained by FSW consists of three distinguishable zones:

1) The nugget zone (NZ), where the combination between severe plastic deformation and high temperature results in recrystallisation.

2) The thermo-mechanically affected zone (TMAZ) between the nugget and the base material, where the microstructure suffers plastic deformation and heating, but without the onset of recrystallisation and

3) The heat-affected zone (HAZ), a region of the base material which experiences heating but does not undergo any plastic deformation [3].

The heat generated during FSW modifies the preceding array of precipitates and the different thermal cycles experienced in each weld zone are, therefore, responsible for different behaviours in a corrosive environment. Many studies reported localized corrosion phenomena in various regions of aluminium friction stir welds when they were

exposed to chloride containing electrolytes[4-11]. For instance, Bousquet et al. [4] reported that the HAZ of friction stir welded AA2024-T3 was most sensitive to corrosion, suffering pitting on coarse intermetallic compounds and intergranular corrosion (IGC) along intergranular S' and S phase precipitates (coherent and incoherent Al_2CuMg). On the other hand, Lumsden et al. [10] have shown that the region near the interface between nugget and TMAZ in friction stir welded AA7050-T7651 was most sensitive to IGC and intergranular stress corrosion cracking (SCC) under slow strain rate, due to precipitate coarsening in this area. In a previous study of our group [11], the scanning vibrating electrode technique (SVET) was employed to observe the corrosion behaviour of a dissimilar AA7050-T76511/AA2024-T3 FSW lap joint, revealing that more intense pitting occurred at the nugget of AA7050. IGC occurred more deeply at the AA2024 HAZ, after longer exposure times. In summary, friction stir welds can often be considered regions of diminished corrosion resistance in a welded structure, due to coarsening and dissolution of precipitates.

The alloying elements and the hardening heat treatments applied to aluminium high strength alloys have the potential to impair their corrosion resistance [12, 13]. Therefore, such alloys are usually anodised to improve corrosion resistance or to allow better adhesion of protective paints. In acidic electrolytes, such as sulphuric, chromic, oxalic and phosphoric acids, a porous-type anodic layer is obtained and its thickness is linearly proportional to the charge involved in the electrochemical reaction, *i.e.*, to the anodisation time under galvanostatic conditions [14]. When the substrate for anodic oxidation is pure aluminium, the classical structure of hexagonal-shaped, regular cells with a pore in the centre of each cell is obtained [15]. However, if a highly alloyed substrate is employed, the properties of the anodic layer are no longer the same and the occurrence of defects is observed as a result of the existent intermetallic compounds. Fratila-Apachitei *et al.* [16]

reported that Al_2Cu particles are rapidly dissolved on the metal–oxide interface during sulphuric anodising of a cast AlSi10Cu3 alloy, because of their solubility in the acid electrolyte, leaving voids in the oxide. On the other hand, Al-Si and Al-Si-Fe precipitates have been reported to remain entrapped in the anodic oxide of commercially pure aluminium substrate, with preferentially oxidised surroundings [17]. Saenz de Miera *et al.* [18] have shown that Al-Cu-Mg-containing particles were removed from the surface of AA7075-T6 by anodising in sulphuric acid, while Al-Cu-Fe-containing particles remained on the surface. In general, higher contents of alloying elements can cause defects in the anodic oxide, which result in loss of mechanical properties and corrosion resistance.

Anodising of Al-alloy panels usually is done before final assembly procedures in the aircraft industry. However, when riveting is replaced by FSW, anodic oxide layers are removed by the tool friction and then an anodising (or reanodising) step should follow the welding process. Although FSW and anodisation are widely studied processes, the interaction between these two techniques has not yet been properly examined. The consequences of the severe microstructural changes imposed by FSW on a subsequent anodisation should be thoroughly investigated, considering that both processes are of particular interest for high strength aluminium alloys. Since the microstructure of the substrate influences the morphology and properties of the anodic oxide [19], anodised friction stir welds may have a different corrosion resistance.

In this study, an FSW lap joint between an AA2024-T3 plate and an AA7050-T76511 L profile was anodised in sulphuric acid electrolyte. The morphology of the obtained anodic oxide was characterised by microscopic techniques and the corrosion resistance was investigated by SVET under simultaneous polarisation.

2. Experimental

A lap joint between an AA2024-T3 sheet and an AA7050-T76511 extruded profile was friction stir welded using a welding speed of 960 $mm \cdot min^{-1}$ and a rotation speed of 1700 rotations per minute, as in a previous study [11]. This assembly represents the joint between an AA7050 stringer and the AA2024 skin of an aircraft, where the AA2024 alloy faces outwards and the AA7050 faces the inner side of the aircraft [20, 21]. During welding, the AA7050 profile was facing the tool. A schematic drawing of the welding process is shown in **Fig. 1**. The chemical composition of AA7050 was determined by optical emission spectroscopy as 6.16 wt. %Zn, 2.06 wt. %Cu, 1.88 wt. %Mg, 0.14 wt. %Fe, 0.10 wt. %Zr, 0.07 wt. %Si, <0.21 wt. % other elements and balance aluminium.

INSERT Figure 1

Prior to anodising, samples from the weld region were sanded with SiC paper and polished with 1 µm diamond paste, using neutral soap as lubricant. The surface of the AA7050 had a rough irregular layer, due to the contact with the rotating tool and, for this reason, around 100-200 µm of the thickness were removed by the surface preparation. Thereafter, samples were ultrasonically cleaned in ethanol for 5 min. Porous anodising was performed using a current density of 14 mA cm^{-2} in 15 %wt. H_2SO_4 electrolyte for 25 min under stirring and controlled temperature of 20 ºC, in accordance with the SAE AMS2471-H standard [22], but avoiding a final sealing step. Immediately after anodising, samples were rinsed with demineralised water, air-dried and stored in a vacuum desiccator.

Prior to anodising, the Vickers hardness of the polished AA7050 surface was measured across the weld path at 200 µm intervals with a load of 300 gf. To verify the thickness of the anodic oxides obtained, the anodised specimens were glued with epoxy resin on aluminium sheet pieces of the same size, forming a “sandwich”. After that, cross-sections

were cut, sanded and polished as previously described. The cross-sections were examined with an *Olympus BX51* optical microscope with image acquisition and measurements of anodic oxide thickness were taken 30 µm distant from each other, using the *ImageJ* software. In some cases, samples were exposed for 20 s to Keller's reagent (2.5 mL HNO_3, 1 mL HF, 95 mL H_2O), to reveal the substrate microstructure. A *Zeiss EVO MA10* scanning electron microscope (SEM) equipped with energy dispersive X-ray spectroscopy (EDS) was employed for both surface and cross-section sample examination.

To investigate corrosion resistance, current maps of the surface of anodised specimens exposed to 0.1 M NaCl were acquired using an *Applicable Electronics* SVET system. In order to accelerate corrosion phenomena, the samples were anodically polarised to +20 mV above the pitting potential (E_{pit} = -410 mV *vs*. the standard hydrogen electrode - SHE) of the AA7050 base material [11] during the current acquisition scans (i-maps). The scanning microelectrode was a Pt/Ir wire with a 10µm diameter tip, vibrating with an amplitude of 2 µm at a distance of 50 µm from the sample surface. An *Autolab PGSTAT 128N* potentiostat was used to polarise the samples, employing a Pt wire as counter electrode and a 0.1 M Cl^- Ag/AgCl electrode ($E_{Ag/AgCl}$ = +281 mV *vs*. SHE) placed directly in the electrolyte. For this purpose, an Ag wire (*Aldrich*, 99.99 %Ag) was chloridised by applying an overpotential of +100 mV *vs.* $E_{Ag/AgCl}$ and checked against a commercial Ag/AgCl electrode before each experiment. However, for simplification purposes, all the potential values mentioned in the text refer to SHE. The sample surface exposed to the electrolyte was limited using a 65 µm thick scotch tape (*3M Inc*.) and fine adjustments were made with epoxy resin, resulting in areas ranging from 7 to 11 mm^2.

All tests and measurements (SVET, oxide thickness profiles, hardness profiles, anodising cell voltage transients) were repeated at least three times.

3. Results

Fig. 2 shows optical micrographs of the base material alloy, the joint and its surroundings. The top view of AA7050 (**Fig. 2a**) shows an elongated grain structure, longitudinally aligned to the extrusion direction of the welded profile. **Fig. 2b** shows a cross section of the weld. It can be seen that the AA7050 profile has a different grain structure near the surface, characterised by coarser grains within a layer of ≈180 µm at the outer side and ≈ 600 µm at the side in contact with the AA2024 sheet. This structure results from the recrystallisation and growth caused by extrusion followed by the T76511 heat treatment (solubilisation, stretching and overageing) of the AA7050 alloy [23]. The typical FSW zones "nugget, TMAZ, HAZ and BM" can be recognized in the cross section in **Fig. 2b** or on the top view in **Fig. 2c**. The line representing the frontier between HAZ and BM was arbitrarily drawn, since no sharp difference between the microstructure of the two zones can be seen in the cross section or on the weld top view on the AA7050 side (**Fig. 2c)**. This surface faces the tool during FSW and receives the most intense heat and deformation, losing its protective anodic oxide. For this reason, the corrosion resistance of the welded and anodized AA7050 side was studied in a first approach. Large voids with diameters around 10 µm aligned in the material flow direction are produced in the outer nugget region during stirring by the welding tool (**Fig. 2d**). These defects may result from non-ideal process conditions [1], such as a too low rotation speed, providing insufficient temperature and ductility of the alloy [24]. Further examination of inner regions of this type of joint can be found in a previous study [11].

INSERT Fig. 2

The microstructure of AA7050 revealed by SEM on the top surface is shown in **Fig. 3**. In the base material (**Fig. 3a**), the larger precipitates have a diameter of circa 2 µm and are aligned with the hot-rolling and extrusion directions. These precipitates were not dissolved

during the heat treatment, as expected for coarse precipitates formed during solidification. EDS analysis of their elemental composition ($Al_{7.4}Cu_{1.8}Fe$) allows the identification of these precipitates as Al_7Cu_2Fe intermetallics. Al_7Cu_2Fe is a common cathodic intermetallic in the AA7xxx alloy series and is related to a high Fe content, derived largely from impurities in alloy production [25]. **Fig. 3b** is a top view of the microstructure on the weld nugget. Here, the Al_7Cu_2Fe particles are smaller-sized and randomly scattered by the friction of the tool. Apparently, these precipitates suffered partial solubilisation during FSW, because of high temperature and intense deformation imposed. In addition, small, elongated precipitates appeared in the NZ after welding. Considering that the dimensions of these particles are circa 100 x 700 nm, EDS analysis was not employed as a quantitative method, since a significant part of the output signal comes from the surrounding matrix. Nevertheless, EDS measurements on these particles revealed at least two times greater Mg and Zn contents in comparison to the matrix, specially under low beam acceleration voltage (10 kV) and reduced sampling volume, indicating that these precipitates are in fact $MgZn_2$ (η). Very fine particles with the same mass contrast are also found in the base material (**Fig. 3a**) and it can be inferred that these are η precipitates as well, although in this case they appear to be much smaller (≈ 250 x 250 nm) and in lower number. It should be mentioned that Al_7Cu_2Fe and η are the most commonly found precipitates in AA7050 alloys [26, 27]. Voids associated with metal stirring and precipitate fragmentation are present on the surface of the nugget zone, such as in **Fig. 2d**. The mass contrast in the SEM backscattering electron imaging mode is expected to be brighter for the AA7050 compared to the AA2024, due to its higher density. The analysis of mass contrast and elemental composition of the matrix shows that the vertical flow of AA2024 material in the weld does not reach the upper AA7050 surface and, as found in a previous work [11], is restricted to regions very close to the interface between the two alloys.

INSERT Fig. 3

INSERT Fig. 4

The microhardness profile (**Fig. 4**) across the weld path has the typical "W" shape associated with welded age-hardenable Al alloys [28]. In a very narrow zone of around 1mm on the TMAZ-HAZ border there is a slight hardness drop from 190 to 170 HV due to precipitate coarsening. This agrees with low process temperature and tool rotation speed during FSW. Moreover, in the middle of the nugget zone there are some isolated low hardness points, where values as low as 140 HV could be measured with asymmetrical indentations. Thus, these apparently soft regions are actually explained by superficial elongated stirring voids, as the ones shown in **Fig. 2d**.

Cell voltage transients during anodising were acquired for BM and for welded specimens. From the results obtained, one typical voltage transient for each type of substrate is shown in **Fig. 5**. The inset plot shows the whole 25 minutes of anodisation, while the bigger plot is a closer look at the first 60 seconds. During the first circa 10 seconds, the voltage rises in quasi-linear time dependence, as expected for the initial formation of a barrier-type oxide layer at a constant growth rate. Comparing base material and the weld surface, which comprises nugget, TMAZ and HAZ, no considerable difference can be found at this part of the curve. After the first 10 seconds, voltage deviates from linearity, as a result of the morphological instability that initiates pore formation [29]. At this point, a voltage peak is verified only for the anodising of the base material, whereas for the welded specimens there is a smooth transition. This peak can be attributed to the nucleation of the first pores in the oxide, reducing the existing barrier-type layer to a thinner barrier layer at the bottom of the pores, and/or to the lateral growth of the thinned area [30]. A smoother transition to a porous type layer suggests that pore formation may be facilitated on the welded substrate, originating from voids or cracks in the barrier oxide, resulting from

abundant defects and microstructural heterogeneities in the weld. From pore formation up to the conclusion of anodising (**Fig. 5**, inset plot), the welded specimens displayed a lower cell voltage, i.e. a lower electrical resistance for the entire oxide, which can be explained by a more defective oxide in the weld region. The cell voltage at 50 seconds of anodising was chosen as a parameter for comparing stationary voltage values. At this point, the cell voltage was 15.8 ± 0.1V for BM and 15.0 ± 0.25 V for welded samples. Even though, the voltage after pore formation is not truly stationary and decreased with longer anodising times. All welded samples presented lower cell voltages than BM samples until the completion of anodising.

INSERT Fig. 5

INSERT Fig. 6

Figs. 6.a-e show cross-section micrographs of specimens anodised during 25 min in the sulphuric acid bath. The porous oxide layers obtained on the base material achieved a thickness of around 12 µm (**Fig. 6a**). At some points, voids in the oxide layer could be found in association with increased thickness (**Figs. 6a** and **d**). These voids have a diameter compatible with that of Al_7Cu_2Fe precipitates found in the alloy, indicating that these precipitates are dissolved during anodising. According to Fratila-Apachitei et al. [17], whenever the substrate-oxide front encounters copper-rich particles the current distribution changes promoting rapid oxidation and dissolution of these particles, due to their lower resistivity compared to that of the oxide. The voids in **Figs. 6a** and **d** are filled with a lower mass-contrast material with the same elemental composition determined by EDS as that of the oxide layer (Al, O and low concentrations of S) and is thus Al oxide or hydroxide with a lower apparent density than tubular Al_2O_3 formed on other sites. This oxide accumulates on the void side facing the metal and can be attributed to the selective dissolution of Cu and Fe from the precipitate, forming an irregularly porous and more

permeable alumina structure deposited on the dissolution front. The oxide front does not seem to advance more rapidly on the Al_7Cu_2Fe/oxide interface compared to the Al-matrix/oxide one (**Fig. 6b**). However, after complete Al_7Cu_2Fe particle dissolution and further formation of tubular porous alumina, the oxide front advances more rapidly and the final total film thickness is greater where these particles dissolve. This is compatible with an oxide film formation controlled at least partially by migration or diffusion transport of species along the regular tubular pores of the alumina film.

The partially filled voids resulting from Al_7Cu_2Fe dissolution may impact on the mechanical properties of the oxide, nevertheless the corrosion resistance is not directly affected, as the oxide film is thicker on these sites (**Fig 6a** and **d**). Voids related to precipitate dissolution were also found in oxides obtained on welded specimens, although they were smaller in that case, in accordance with the findings that precipitates are finer in the nugget zone (**Fig. 6c**). **Fig. 6e** exhibits another type of defect encountered in the anodized nugget zone. Previously existing cracks and porosities created during FSW allow the electrolyte to penetrate, producing an irregular oxide layer. This kind of oxide protrusion into the NZ metal can certainly act as a crack initiator, indicating that the adequate removal of stirring voids is necessary to maintain the fatigue strength of the material.

In comparison with the oxide layer on the BM(**Fig. 6a**), the oxide layer on the TMAZ (**Fig. 6b**) is around 20% thicker. On the NZ (**Fig. 6c**) the oxide thickness varies, with values down to 50% of the oxide thickness found on the BM. Furthermore, the oxide thickness measurements performed by optical microscopy perpendicularly to the FSW joint (**Fig. 7**) show that the oxide film forms faster in regions where the hardness is lower.

INSERT Fig. 7

INSERT Fig. 8

The shape of the substrate/oxide interface seems to vary depending on the substrate (**Fig. 8**). On the base material (**Fig. 8a**), HAZ and TMAZ (**Fig. 8b**) the oxide front is flat, except for occasional protuberances related to the dissolution of coarse Al_7Cu_2Fe particles, whereas the oxide front on the nugget zone (**Fig. 8c**) is rougher with protuberances even in areas where no cracks or porosities were left by FSW. As a result, the optical brightness of the BM, HAZ or TMAZ polished surfaces is not significantly affected by anodising (still some opacity is produced), while the NZ (formerly not visually detectable) darkens due to metal/oxide interface roughening.

In order to study the protective nature of the anodic oxide film produced on the weld surface of AA7050 (*i.e.*, xy-plane in **Fig. 1**), current density maps were acquired using SVET with simultaneous anodic polarisation of -390 mV/SHE. It is important to note that the applied potential lies only 20 mV above the pitting potential of AA7050 [11] and is applied to accelerate the occurrence of localised corrosion on less protective oxide film sites. Several anodised FSW samples were analysed during exposure in 0.1 M NaCl solution and the corresponding current density maps always showed the nucleation of localised corrosion in the NZ. A typical series of acquired current density maps is presented in the example of **Fig. 9** that showed among other specimens a clearer time separation of individual pitting events.

The exposed area (**Fig. 9a**) extended laterally from the nugget's centre (advance side) to a point on the base material region, comprising from left to right: nugget zone, TMAZ, HAZ and base material. The area framed by the dashed line represents the portion of the original surface scanned during the measurements. To better understand the results, this picture was converted to a binary image (**Fig. 9b**) and overlaid on current density maps. Although the maps were acquired every 15 minutes, only the maps considered more relevant will be

discussed (**Figs. 9c-f**). In addition, the total current was acquired by the potentiostat and a plot of global current density (considering the whole area exposed to the electrolyte) over time is shown in **Fig. 10a**. The comparison between global current density plots and SVET maps facilitates the interpretation of both results and provides information from corrosion events outside the area scanned by SVET.

INSERT Fig. 9

The acquisition of the map in **Fig. 9c** started after 2 h of exposure to the electrolyte. The maps acquired before that time showed little activity. The global current density is practically zero during the first 1.5 h of test (**Fig. 10a**). Thus, there appears to be an incubation period, during which slow processes occur, such as the withdrawal of air from the oxide pores and their filling with electrolyte and the migration of Cl^- ions through the barrier layer at the bottom of the pores. Next, the current starts rising slowly, which may be the manifestation of oxidative processes caused by the penetration of Cl^-. Right before 2 h of test, the current reaches a sudden peak. This peak is attributed to pitting corrosion and, therefore, the anodic region on the nugget in **Fig. 9c** can be identified as the site of the first pit.

Fig. 9d shows the current density map scanned 2.5 h after the beginning of the test. The first pit continues to be active, and now we have a second strongly anodic zone at the frontier between the nugget and the TMAZ, with currents reaching 800 $\mu A \cdot cm^{-2}$. In addition, another anodic region is seen in the lower left corner of the map. The positive currents measured in that place may originate in a corrosion event happening outside the scanned area. Both new anodic zones seem to be caused by nucleation and growth of pits. This is confirmed analysing the optical micrograph of the sample after the test, **Fig. 9g**, where the two pits can be seen. In the diagram displaying the global current density (**Fig. 10a)**, one peak is found right before the beginning of that scan (2.5 h) and one right after.

Considering that each scan took 7 minutes, both of them could be caused by both pits. The next two maps (**Figs. 9e** and **f**) indicate repassivation of the pit at the lower left corner, as well as a modification of the shape of the first anodic zone. With support of **Fig. 9g**, it can be said that this anodic zone changed its shape because new pits nucleated adjacent to the first one.

As seen in **Fig. 9g**, pitting corrosion occurred in the nugget zone and at the frontier between nugget and TMAZ. In fact, the nugget zone and its frontier with TMAZ on the advance side presented an anodic oxide layer with thickness as little as 50% of the values encountered on other zones and on the base material (**Figs. 6a-c**, **Fig. 8**). Since these regions have a thinner porous oxide layer, the permeation of electrolyte is expected to occur faster, allowing earlier penetration of Cl^- anions and degradation of the barrier layer. From then on, metal dissolution is promoted by Cl^- and pitting corrosion begins. Accordingly, defects in the porous layer on these regions may ease the penetration of Cl^- [31] and hence promote pitting. It can be noted that the pits found in the nugget region of **Fig. 9g** are localised mainly on the arched lines present in the nugget. These lines become apparent after anodising and are the same shape as the stirring voids.

The evolution of current density in time for single pits can be derived from the analysis of sequential SVET current density maps. The positive current densities were integrated over each pit shown in the SVET maps of **Fig. 9** and are presented on the same time scale in **Fig. 10b**. After nucleation, the indirectly calculated pit current grows approximately linearly with time, reaching a maximum value of slightly above 2 µA/pit. Comparing **Fig. 10a** (global current density) with **Fig. 10b** (calculated individual pit currents), it is possible to see that pit current rises are in good agreement with global current density rises, but show individual values which are roughly two orders of magnitude lower than the values of the global current density related to the total sample area at the same time. If

the exposed area of $11.6 \cdot 10^{-2}$ cm^2 is considered, the global current still results in values 10 µA < I < 40 µA) which are one order of magnitude higher than the integrated pit currents calculated from SVET maps.

4. Discussion

With exception of the locations where coarse precipitates were dissolved, flat interface (**Fig. 6a, b**) and constant oxide thickness **(Fig. 8a, b**) were found for the base material, HAZ and TMAZ. This is expected if the porous oxide formation rate is controlled by the same process along the metal/oxide interface. The transport of species across the barrier oxide on the bottom of the oxide pores has been considered as the rate determining step during the initial stages of oxide formation [32]. As the oxide layer grows, we can expect that transport processes by diffusion or migration along these pores will increasingly limit the formation rate. This could explain the fact that the oxide front of thicker layers does not advance significantly faster during the dissolution of coarse Al_7Cu_2Fe precipitates (**Fig. 6b**). However, after dissolution of Al_7Cu_2Fe and formation of a less dense oxide or hydroxide filling the dissolution void of the precipitate, transport is favoured and the film formation becomes faster resulting in a locally thicker AO layer (**Figs. 6a** and **d**).

Size and distribution of precipitates may influence the anodic film formation. As formerly shown in some studies, the oxidation behaviour of intermetallics in H_2SO_4 generally differs from that of the metallic matrix, leading to a locally faster advancing metal/oxide front in the case of Cu-containing intermetallics [16, 18] or to local blocking of alloy oxidation as in the example of Si and Fe rich intermetallics [17]. Therefore, during the anodisation inhomogeneous current distribution and oxide thickness would be expected.

In the present work, compared to the oxide on the BM , thinner oxide layers with rough interfaces were observed on the nugget zone where Al_7Cu_2Fe intermetallics are smaller

sized due to crushing and redissolution, while partially coherent or incoherent η are at a higher concentration. Besides that, thicker oxide layers are found on HAZ and TMAZ, where the hardness is lower (**Fig. 4)**, and thus, dissolution of $MgZn_2$ GP zones (Guinier-Preston zones) and coarsening of η took place. This indicates that these two precipitates affect the oxide layer formation rate differently. The wavelength of the metal/oxide interface roughness is in the same order of magnitude as that of the distance between neighbouring η precipitates (hundreds of nm). Possibly, fine $MgZn_2$ precipitates are pinning the oxide front advancement due to their slower dissolution, limiting the final AO thickness on the NZ.

Another important characteristic of FSW, which might influence anodic film formation, is the strong plastic deformation, especially in the TMAZ, where the effect of plastic deformation is not mitigated by recrystallisation. However, recently published studies with pure aluminium deformed up to 80%, showed that this had no effect on the thickness of porous anodic oxide films [33]. The same observation was made with Al 99.1% anodised after deformation by ECAP (equal channel angular pressing) [34]. This process causes crushing of intermetallics like FSW, however, unlike FSW, cold working by ECAP does not interfere in the distribution of alloying elements present in the matrix and in second phase particles, respectively. This distribution, however, has considerable influence on anodic film formation. For the alloying element Cu in solid solution, accumulation beneath the oxide [35] and higher voltage during galvanostatic anodising [36] indicate that a higher driving force is necessary than in the absence of Cu. For Al-Zn-Mg alloys, on the other hand, it has been reported that the anodisation voltage is lower, when the alloying elements are in solid solution [37]. The voltage transients for galvanostatic sulphuric anodization in the present work are slightly lower for the films grown on AA7050 in the weld region, when compared with the base material. Recrystallisation occurring during

FSW points to elevated temperatures, at which the solubility of alloying elements is considerably higher. Even the strong plastic deformation might contribute to enhanced solubility, effect which is used in mechanical alloying [38], although no data are available for the case studied here.

As verified by the SVET measurements for samples polarised slightly above E_{pit}, the thinner porous oxide layer combined with the presence of defectively anodised FSW stirring voids decreases the resistance to pitting on the NZ (**Fig. 9**). From sequential SVET maps, it was possible to determine individual pit currents. Considering the exposed area of $11.6 \cdot 10^{-2}$ cm^2 and the current density values of **Fig. 10**, the global current is around one order of magnitude higher than the added single pit currents. Possible reasons for this are the assessment of only a fraction of the total current arising from individual pits at the surface distance where the oscillating electrode tip is placed (50 µm) and the lack of knowledge of the exact conductivity of the electrolyte at the pit opening region. The more concentrated electrolyte at this place and resulting higher local conductivity lead to the underestimation of the actual current densities. Thus, the pit current decay after a maximum does not necessarily reflect the partial repassivation of the pit, as the enrichment of the electrolyte species near the pit mouth locally increases the electrolyte conductivity with time, resulting in underestimated current density if the global electrolyte conductivity is used for its calculation.

The results showed that, after sulfuric anodising, a higher corrosion susceptibility is observed at the nugget zone in comparison to the other weld zones. Nevertheless, the use of other anodising bath formulations might produce oxide layers less sensible to substrate microstructure variation. Also, the sealing of oxide layers should be studied aiming to lower sensibility of the oxide film thickness and defect density with respect to variations of the metal matrix microstructure.

5. Conclusions

The most remarkable aspects of the porous anodisation layers obtained on FSW samples are the thickness variations along the characteristic weld zones and the increased roughness in the metal/oxide interface on the nugget zone. These two facts determine the lower corrosion resistance of the nugget zone.

Coarse Al_7Cu_2Fe intermetallics in the AA7050 alloy dissolve faster than the matrix. This dissolution seems not to affect corrosion resistance, as the overall oxide thickness is locally higher at that site. On the other hand, the NZ with higher density of fine η ($MgZn_2$) precipitates has a thinner oxide layer with a rough metal/oxide interface.

Besides the thinner oxide layer on the NZ, the corrosion resistance on this zone can be further reduced by the presence of stirring voids produced during the FSW process, which are later irregularly covered during the anodising process.

Individual pit current transients were obtained from sequential SVET maps, but comparison with the global current values shows that calculated values are strongly underestimated due to local increase of the conductivity.

Acknowledgements: The authors would like to acknowledge CAPES for financial support, *EMBRAER* (São José dos Campos - Brazil) for welding the alloys specially for this study and *CMM-UFRGS* for the use of microscopy facilities.

REFERENCES

[1] B.T. Gibson, D.H. Lammlein, T.J. Prater, Friction stir welding: Process, automation, and control, Journal of Manufacturing Processes, 16 (2014) 56-73.
[2] T.U. Seidel, A.P. Reynolds, Visualization of the material flow in AA2195 friction-stir welds using a marker insert technique, Metallurgical and Materials Transactions A, 32A (2001) 2979-2884.
[3] R.S. Mishra, Z.Y. Ma, Friction Stir Welding and Processing, Materials Science and Engineering, R 50 (2005) 1-78.
[4] E. Bousquet, A. Poulon-Quintin, M. Puiggali, O. Devos, M. Touzet, Relationship between microstructure, microhardness and corrosion sensitivity of an AA 2024-T3 friction stir welded joint, Corrosion Science, 53 (2011) 3026-3034.
[5] J. Kang, R.-d. Fu, G.-h. Luan, C.-l. Dong, M. He, In-situ investigation on the pitting corrosion behavior of friction stir welded joint of AA2024-T3 aluminium alloy, Corrosion Science, 52 (2010) 620-626.
[6] A. Davoodi, Z. Esfahani, M. Sarvghad, Microstructure and corrosion characterization of the interfacial region in dissimilar friction stir welded AA5083 to AA7023, Corrosion Science.
[7] M. Jariyaboon, A.J. Davenport, R. Ambat, B.J. Connolly, S.W. Williams, D.A. Price, The effect of welding parameters on the corrosion behaviour of friction stir welded AA2024–T351, Corrosion Science, 49 (2007) 877-909.
[8] V. Proton, J. Alexis, E. Andrieu, J. Delfosse, M.-C. Lafont, C. Blanc, Characterisation and understanding of the corrosion behaviour of the nugget in a 2050 aluminium alloy Friction Stir Welding joint, Corrosion Science, 73 (2013) 130-142.
[9] C.S. Paglia, R.G. Buchheit, A look in the corrosion of aluminum alloy friction stir welds, Scripta Materialia, 58 (2008) 383-387.
[10] J.B. Lumsden, M.W. Mahoney, C.G. Rhodes, G.A. Pollock, Corrosion Behavior of Friction-Stir-Welded AA7050-T7651, Corrosion, 59 (2003) 212-219.
[11] J.C.B. Bertoncello, S.M. Manhabosco, L.F.P. Dick, Corrosion study of the friction stir lap joint of AA7050-T76511 on AA2024-T3 using the scanning vibrating electrode technique, Corrosion Science, 94 (2015) 359-367.
[12] F. Song, X. Zhang, S. Liu, Q. Tan, D. Li, The effect of quench rate and overageing temper on the corrosion behaviour of AA7050, Corrosion Science, 78 (2014) 276-286.
[13] W. Zhang, G.S. Frankel, Transitions between pitting and intergranular corrosion in AA2024, Electrochimica Acta, 48 (2003) 1193-1210.
[14] W. Lee, S.-J. Park, Porous Anodic Aluminum Oxide: Anodization Templated Synthesis of Functional Nanostructures, Chemical Reviews, 114 (2014) 7487-7556.
[15] F. Keller, M.S. Hunter, D.L. Robinson, Structural Features of Oxide Coatings on Aluminum, J. Eletrochem. Soc., 100 (1953) 411-419.
[16] L.E. Fratila-Apachitei, J. Duszczyk, L. Katgerman, AlSi(Cu) anodic oxide layers formed in H2SO4 at low temperature using different current waveforms, Surface and Coatings Technology, 165 (2003) 232-240.
[17] L.E. Fratila-Apachitei, H. Terryn, P. Skeldon, G.E. Thompson, J. Duszczyk, L. Katgerman, Influence of substrate microstructure on the growth of anodic oxide layers, Electrochimica Acta, 49 (2004) 1127-1140.
[18] M. Saenz de Miera, M. Curioni, P. Skeldon, G.E. Thompson, The behaviour of second phase particles during anodizing of aluminium alloys, Corrosion Science, 52 (2010) 2489-2497.
[19] J.-h. Liu, M. Li, S.-m. Li, M. Huang, Effect of the microstructure of Al 7050-T7451 on anodic oxide formation in sulfuric acid, International Journal of Minerals, Metallurgy and Materials, 16 (2009) 432-438.
[20] C. Velotti, A. Astarita, A. Squillace, S. Ciliberto, M.G. Villano, M. Giuliani, U. Prisco, M. Montuori, G. Giorleo, F. Bellucci, On the critical technological issues of friction stir welding lap joints of dissimilar aluminum alloys, Surface and Interface Analysis, 45 (2013) 1643-1648.
[21] L. Dubourg, A. Merati, M. Jahazi, Process optimisation and mechanical properties of friction stir lap welds of 7075-T6 stringers on 2024-T3 skin, Materials & Design, 31 (2010) 3324-3330.
[22] SAE AMS2471H, Anodic Treatment of Aluminum Alloys: Sulfuric Acid Process, Undyed Coating, in, SAE International, 2014, pp. 7.
[23] SAE AMS4201F, Aluminum Alloy Plate 6.2Zn - 2.3Cu - 2.2Mg - 0.12Zr (7050-T7651) Solution Heat Treated, Stress Relieved, and Overaged, in, SAE International, 2014, pp. 5.
[24] J. Adamowski, C. Gambaro, E. Lertora, M. Ponte, M. Szkodo, Analysis of FSW welds made of aluminium alloy AW6082-T6, Archives of Materials Science and Engineering, 28 (2007) 453-460.
[25] N. Birbilis, M.K. Cavanaugh, R.G. Buchheit, Electrochemical behavior and localized corrosion associated with Al7Cu2Fe particles in aluminum alloy 7075-T651, Corrosion Science, 48 (2006) 4202-4215.

[26] K. Shen, J.-l. Chen, Z.-m. Yin, TEM study on microstructures and properties of 7050 aluminum alloy during thermal exposure, Transactions of Nonferrous Metals Society of China, 19 (2009) 1405-1409.
[27] C. Mondal, A.K. Mukhopadhyay, On the nature of T(Al2Mg3Zn3) and S(Al2CuMg) phases present in as-cast and annealed 7055 aluminum alloy, Materials Science and Engineering: A, 391 (2005) 367-376.
[28] C.B. Fuller, M.W. Mahoney, M. Calabrese, L. Micona, Evolution of microstructure and mechanical properties in naturally aged 7050 and 7075 Al friction stir welds, Materials Science and Engineering: A, 527 (2010) 2233-2240.
[29] J.Q. Su, T.W. Nelson, R. Mishra, M. Mahoney, Microstructural investigation of friction stir welded 7050-T651 aluminium, Acta Materialia, 51 (2003) 713-729.
[30] Q. Van Overmeere, J. Proost, Stress-affected and stress-affecting instabilities during the growth of anodic oxide films, Electrochimica Acta, 56 (2011) 10507-10515.
[31] V.P. Parkhutik, V.I. Shershulsky, Theoretical modelling of porous oxide growth on aluminium, Journal of Physics D: Applied Physics, 25 (1992) 1258.
[32] M.M. Lohrengel, Thin anodic oxide layers on aluminium and other valve metals: high field regime, Materials Science and Engineering: R: Reports, 11 (1993) 243-294.
[33] W.J. Stępniowski, M. Michalska-Domańska, M. Norek, E. Twardosz, W. Florkiewicz, W. Polkowski, D. Zasada, Z. Bojar, Anodization of cold deformed technical purity aluminum (AA1050) in oxalic acid, Surface and Coatings Technology, 258 (2014) 268-274.
[34] O. Jilani, N. Njah, P. Ponthiaux, Corrosion properties of anodized aluminum: Effects of equal channel angular pressing prior to anodization, Corrosion Science, 89 (2014) 163-170.
[35] M.A. Páez, S.R. Biaggio, R.C. Rocha-Filho, Y. Sepúlveda, J.H. Zagal, A. Monsalve, X. Zhou, P. Skeldon, G.E. Thompson, On understanding the effect of benzotriazole during barrier-film growth on Al-Cu alloys, Journal of Solid State Electrochemistry, 7 (2003) 442-449.
[36] S. Wernick, R. Pinner, The Surface Treatment and Finishing of Aluminium and Its Alloys, Robert Draper Ltd., Teddington, 1964.
[37] L. Bouchama, N. Azzouz, N. Boukmouche, J.P. Chopart, A.L. Daltin, Y. Bouznit, Enhancing aluminum corrosion resistance by two-step anodizing process, Surface and Coatings Technology, 235 (2013) 676-684.
[38] B.S. Murty, M.M. Rao, S. Ranganathan, Proceedings of the First International Conference on Nanostructured Materials Nanocrystalline phase formation and extension of solid solubility by mechanical alloying in Ti-based systems, Nanostructured Materials, 3 (1993) 459-467.

Figure Captions

Fig. 1: Schematic representation of the FSW lap joint between an AA7050-T76511 extruded profile and an AA2024-T3 sheet.

Fig. 2: OM of (a) etched AA7050-T76511 base material, (b) cross section of the lap joint (etched with Keller's reagent) and (c) top view showing weld zones on AA7050 (etched with Keller's reagent) and (d) detail of stirring marks on the surface of the nugget zone.

Fig. 3: a) SEM view with backscattering electron imaging of precipitates in the AA7050-T76511 alloy (a) in the base material and (b) in the nugget zone.

Fig. 4: Vickers hardness profile measured across the friction stir weld path on AA7050.

Fig. 5: Cell potential transients of galvanostatic anodising of AA7050 base material (BM) and friction stir weld (FSW). The inset graph shows the whole 25 minutes of anodisation and the outer graph is a closer look on the first 60 seconds.

Fig. 6: Backscattering SEM imaging of oxide layers grown on the different FSW zones of AA7050 alloy: (a) Base material (BM), (b) Termomechanically affected zone (TMAZ) and nugget zone (NZ). d) Partially oxide-filled void from dissolved Al_7Cu_2Fe precipitate. e) Oxide protusions into stirring voids or depressions on NZ.

Fig. 7: Oxide film thickness across the FSW path on AA7050.

Fig. 8: Cross sections of the oxide/metal interface of anodised (a) base material (BM), (b) thermomechanically affected zone (TMAZ) and c) nugget zone (NZ).

Fig. 9: a) OM view of anodised friction stir welded AA7050 alloy showing area exposed to electrolyte (epoxy window) and area scanned by SVET (dashed line). b) binary image obtained from scanned area in (a) for superposing with current density maps. c-f) Selected sequential current density maps for exposure times of (c) 2.0h, (d) 2.5h, (e) 3.0h and (f)

3.25h. g) Optical micrograph of same sample after an exposure time of 3.75h. Scans were performed with anodic polarisation of -390 mV/SHE, in 0.1M NaCl electrolyte.

Fig. 10: a) Global current density transient of anodised friction stir welded AA7050 during SVET measurements, with anodic polarization of -390 mV/SHE, in 0.1M NaCl. b) Single pit current transients calculated from sequential SVET maps.

Figure 1

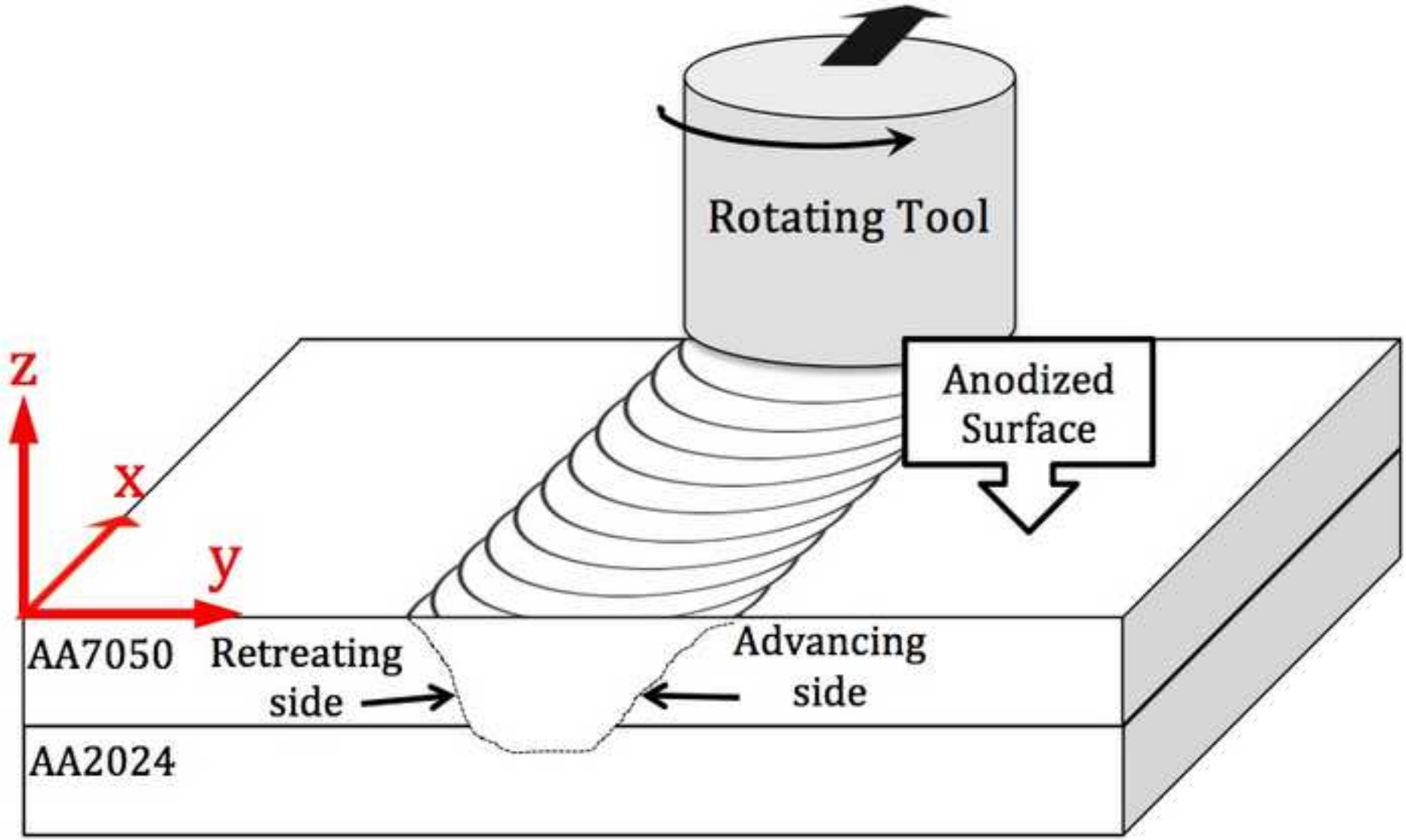
Rotating Tool
Anodized Surface
z
x
y
AA7050
Retreating side
Advancing side
AA2024

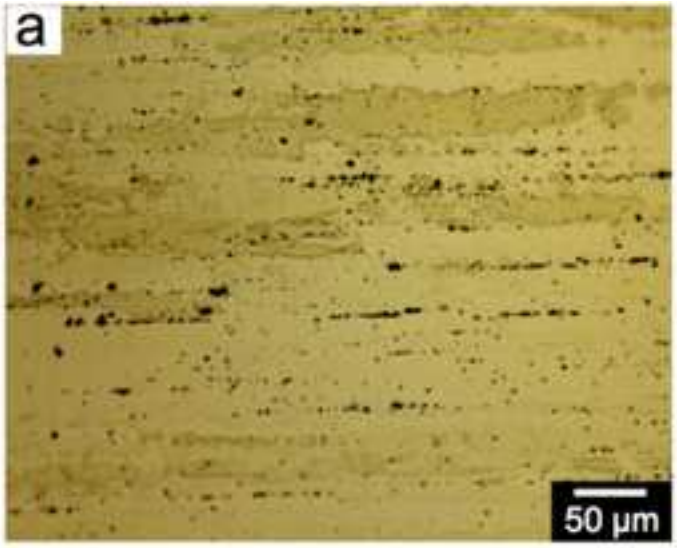

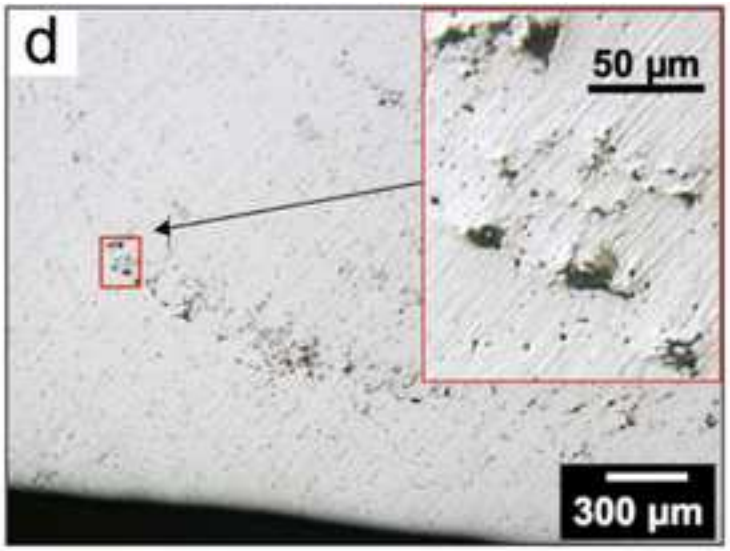

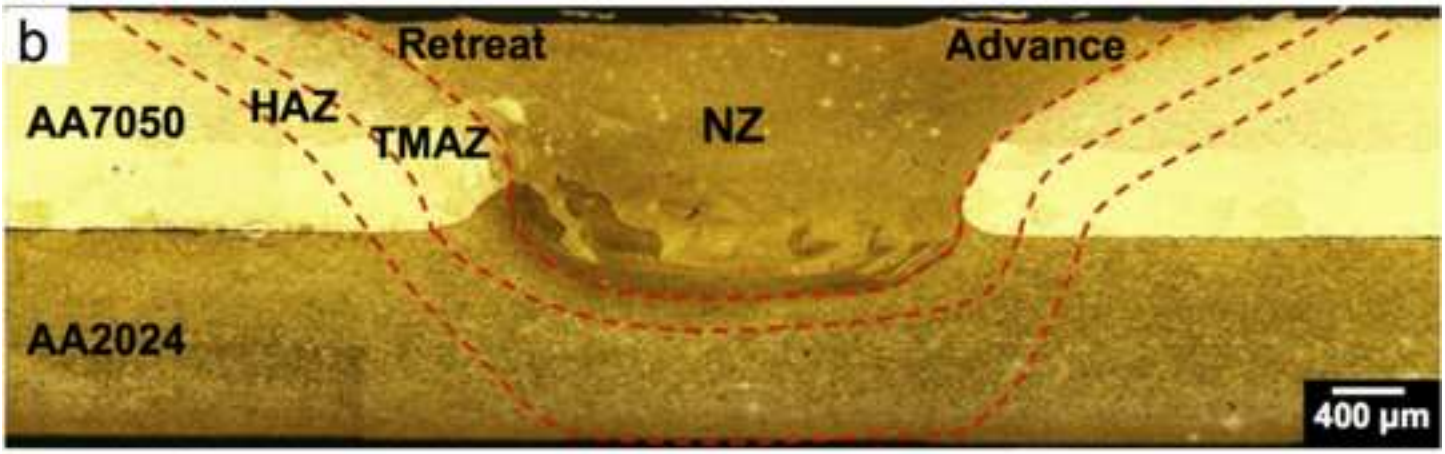

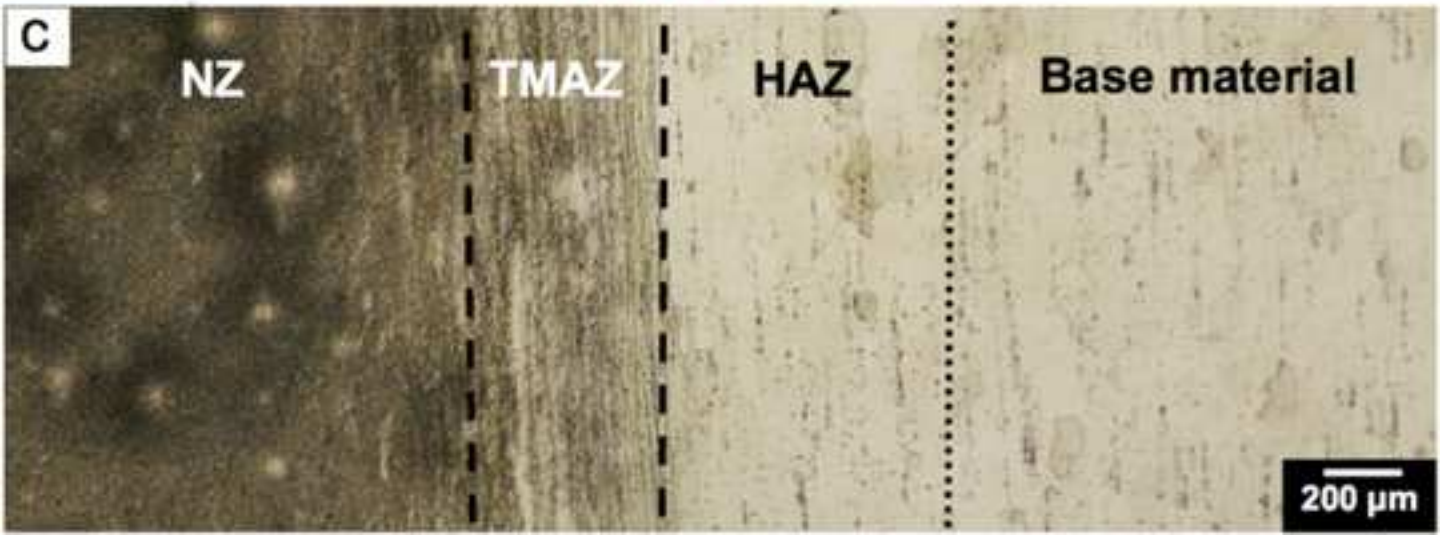

Figure 3

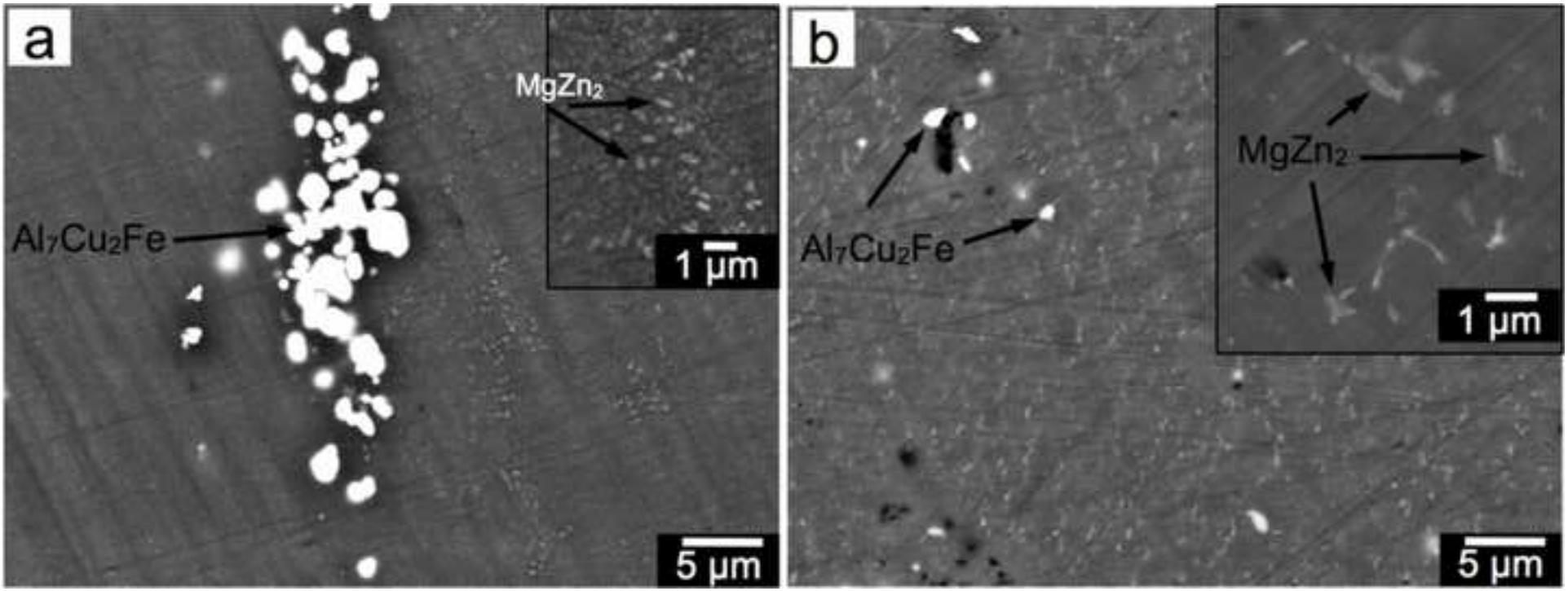

Figure 4

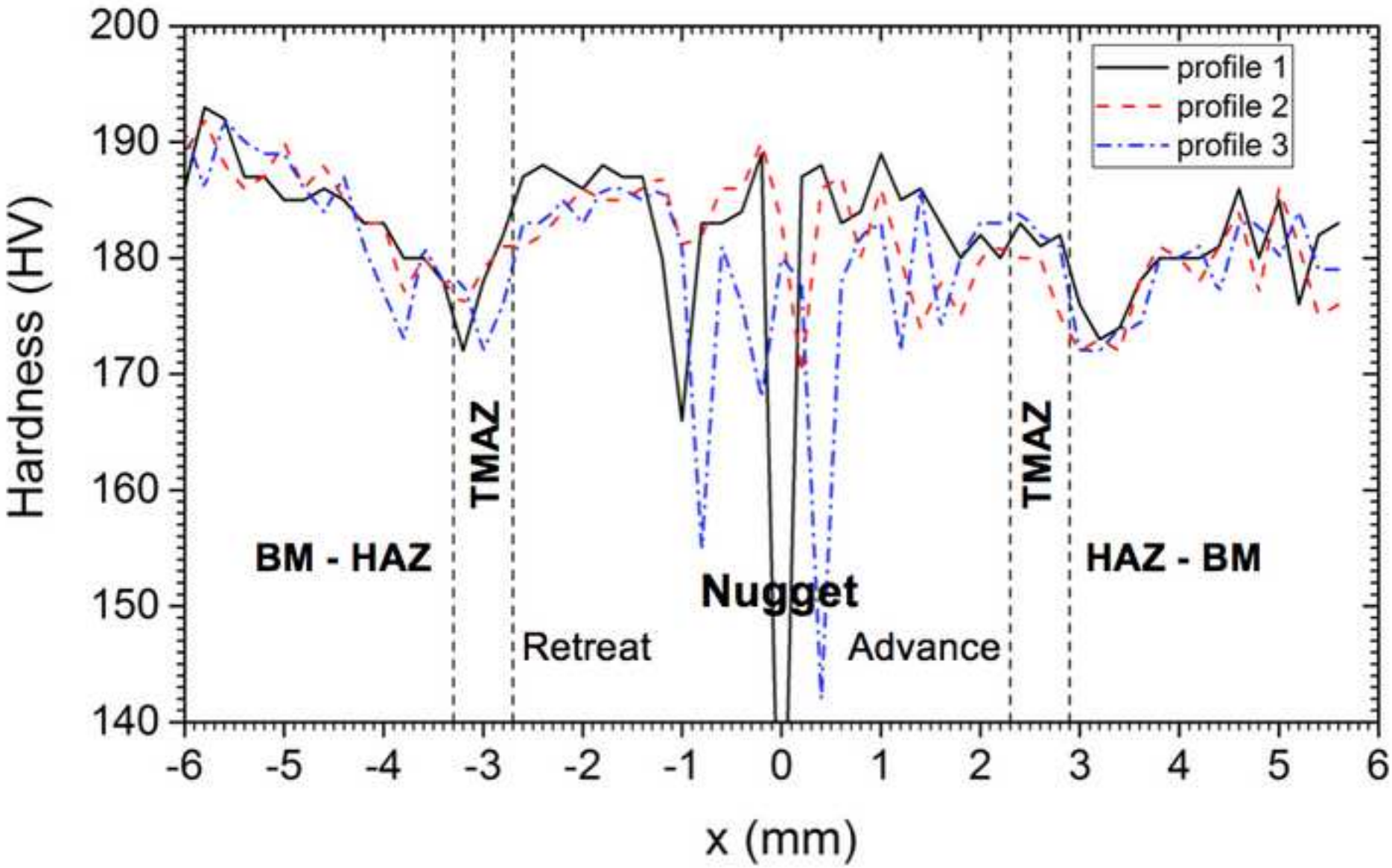
Hardness (HV)
x (mm)
profile 1
profile 2
profile 3
BM - HAZ
TMAZ
Retreat
Nugget
Advance
TMAZ
HAZ - BM
200
190
180
170
160
150
140
-6
-5
-4
-3
-2
-1
0
1
2
3
4
5
6

Figure 5

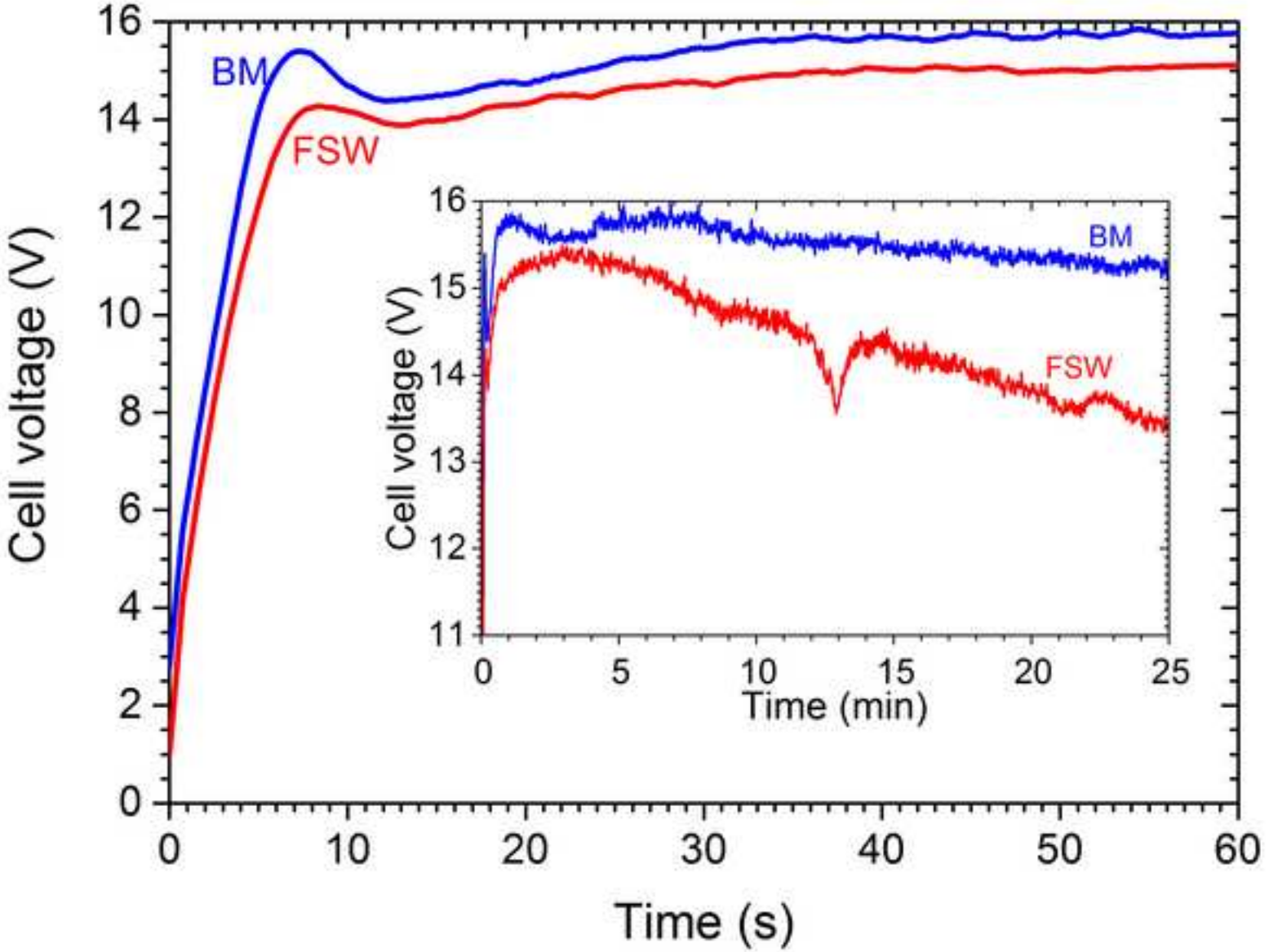
BM
FSW
Cell voltage (V)
Time (s)
0
2
4
6
8
10
12
14
16
0
10
20
30
40
50
60
BM
FSW
Cell voltage (V)
Time (min)
11
12
13
14
15
16
0
5
10
15
20
25

Figure 6

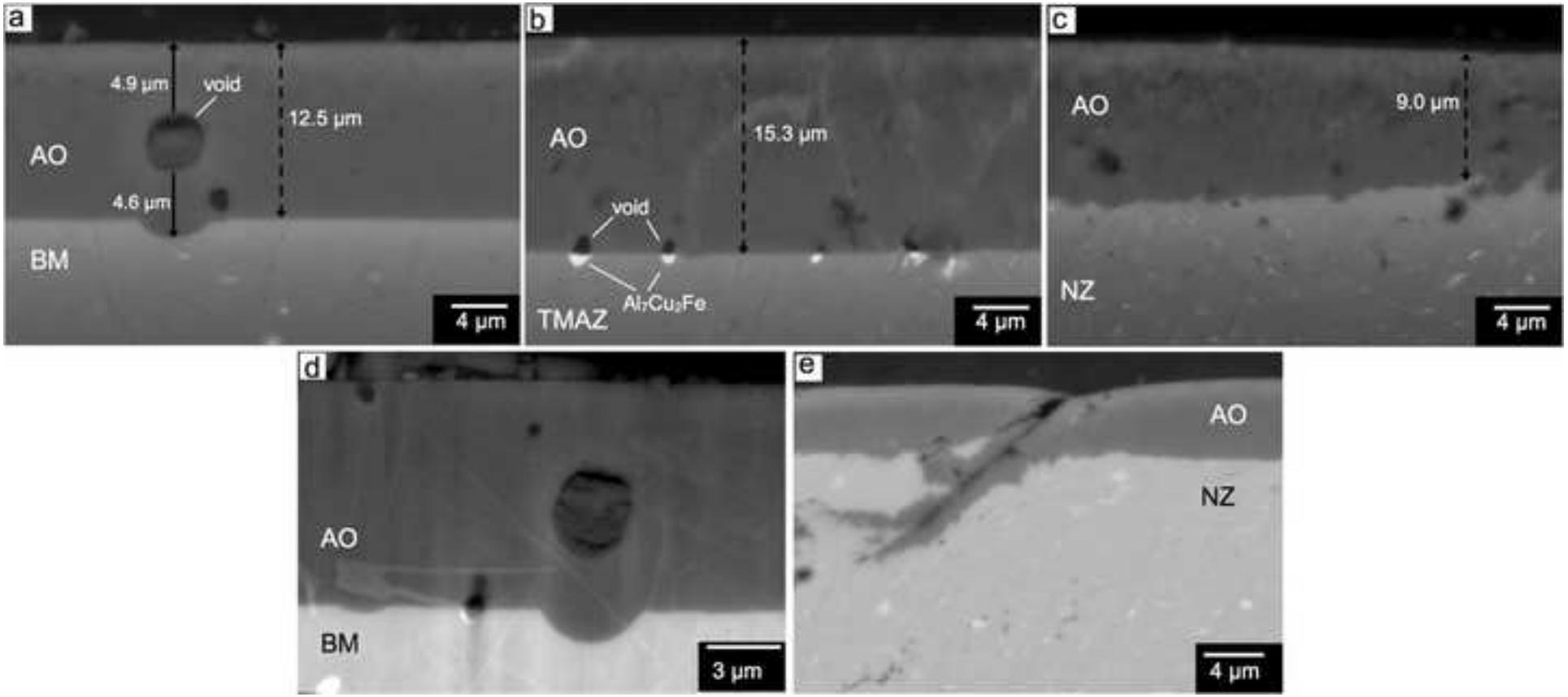
a
4.9 µm
void
12.5 µm
AO
4.6 µm
BM
4 µm
b
AO
15.3 µm
void
TMAZ
Al7Cu2Fe
4 µm
c
AO
9.0 µm
NZ
4 µm
d
AO
BM
3 µm
e
AO
NZ
4 µm

Figure 7

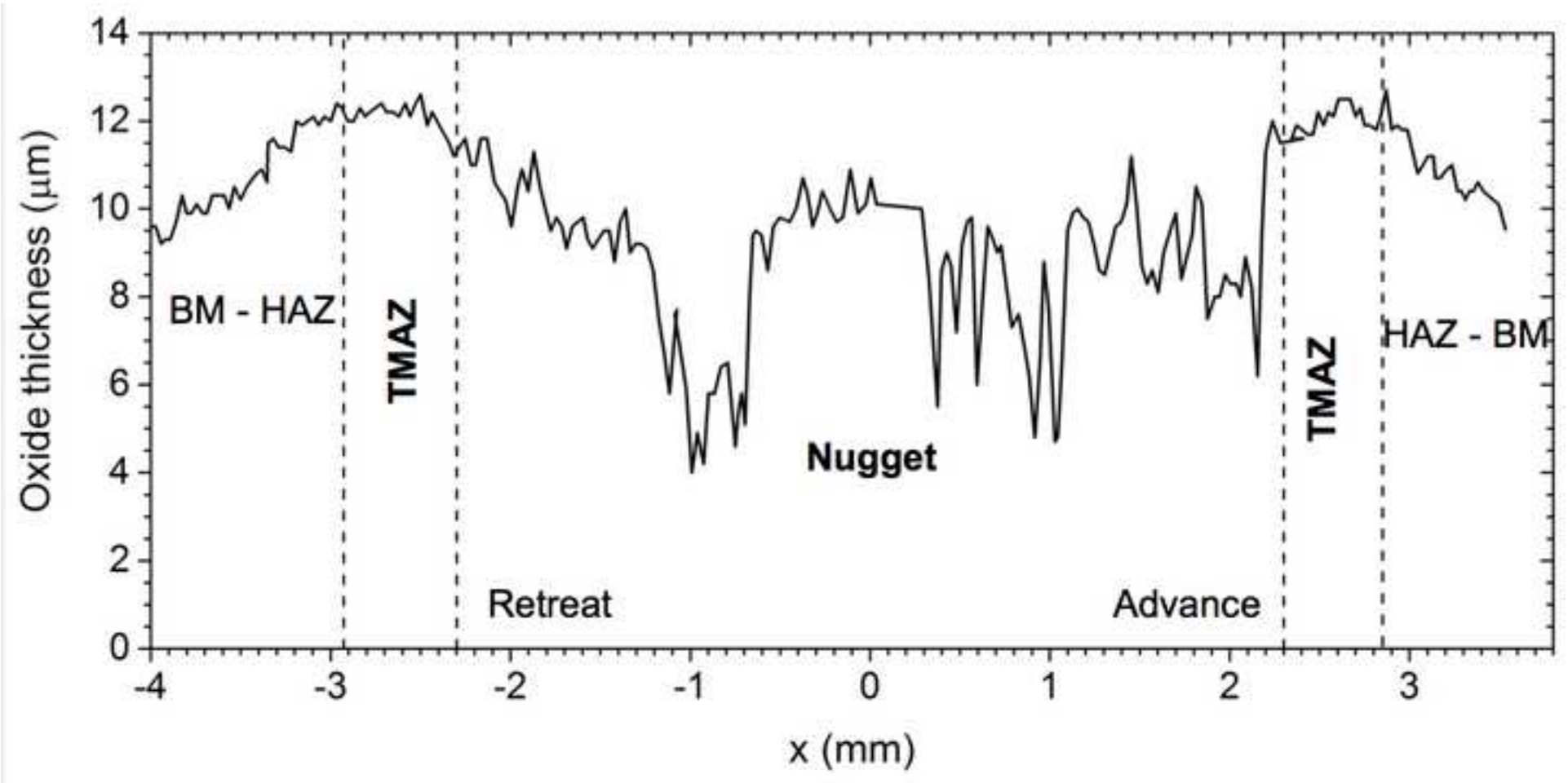
Oxide thickness (µm)
x (mm)
BM - HAZ
TMAZ
Retreat
Nugget
Advance
TMAZ
HAZ - BM
14
12
10
8
6
4
2
0
-4
-3
-2
-1
0
1
2
3

Figure 8

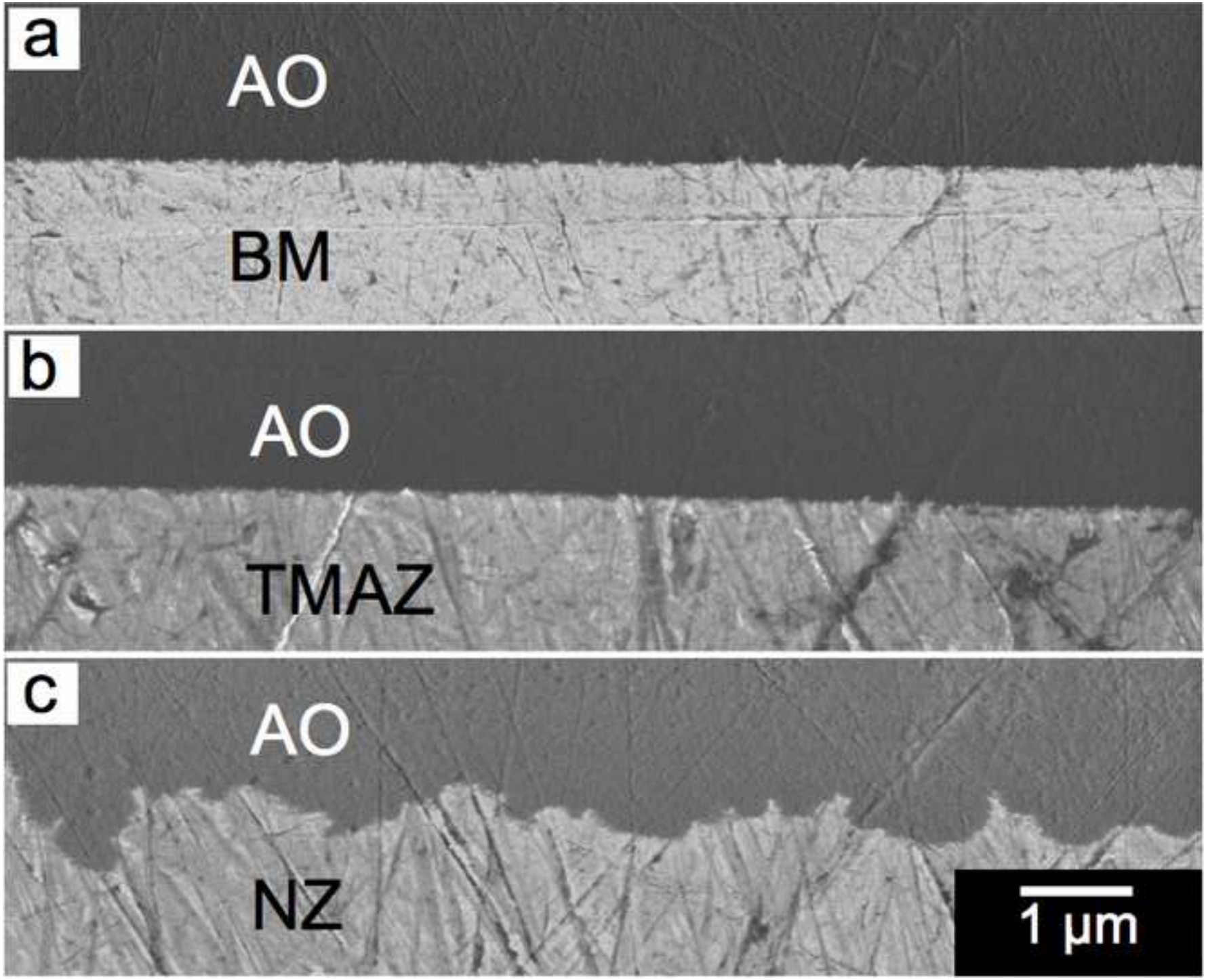

Figure 9